Anisotropy, hysteresis, and morphology of self-patterned epitaxial Fe/MgO/GaAs films

F. Cebollada,[1,*] A. Hernando-Mañeru,[2,3] A. Hernando,[2] C. Martínez-Boubeta,[4] A. Cebollada,[4] and J. M. González[2,3]
[1]*Dept. de Física Aplicada, EUIT Telecomunicación-UPM, Cra. de Valencia, km 7, 28031 Madrid, Spain*
[2]*IMA, Universidad Complutense de Madrid - RENFE, P.O. Box 155, 28230 Las Rozas (Madrid), Spain*
[3]*ICMM-CSIC, Cantoblanco, 28049 Madrid, Spain*
[4]*IMM (CNM-CSIC), Isaac Newton 8 (PTM), 28760 Tres Cantos (Madrid), Spain*
(Received 20 March 2002; revised manuscript received 2 July 2002; published 7 November 2002)

The dependence of the effective anisotropy and of the magnetization reversal processes on the deposition temperature of a series of epitaxial Fe/MgO/GaAs films, grown by a combination of laser ablation and sputtering, has been discussed and correlated to their local morphology and crystallinity. The transverse susceptibility measurements have evidenced the presence of a fourfold effective anisotropy for all films, irrespective of their deposition temperature and local morphology, with a constant value very close to that of single-crystalline iron. The magnetization processes evolve with increasing deposition temperature from a nucleation-expansion-propagation mechanism, taking place in smooth continuous films, to pinning, occurring in self-patterned films with homogeneous distributions of defects, and then to fully isotropic reversal, for tiled films composed of rectangular elements.

DOI: 10.1103/PhysRevB.66.174410 PACS number(s): 75.75.+a, 75.60.Jk, 75.70.−i

I. INTRODUCTION

Nanostructured magnetic materials have drawn a lot of attention in recent years due to the new phenomenology they exhibit and also due to their interest for technological applications, especially for the so-called magnetoelectronic devices.[1–3] The ability to produce this type of device relies in many cases in the design of semiconductor/ferromagnetic heterostructures with tailored magnetic behavior.

The magnetization processes of nanostructured systems depend on their intrinsic properties, which are mainly determined by the crystal-chemical structure, and on extrinsic characteristics such as the system size and morphology, which influence the short-(exchange) and long-(dipolar) range interactions. The progress in the understanding of these processes has been impelled by the study of systems with a high degree of structural and morphological control—e.g., low roughness thin films, nanowires, nanoparticles, or arrays of nanoelements—that can be prepared by a wide variety of growth and patterning techniques such as molecular-beam epitaxy, sputtering, electrodeposition, or pulsed laser deposition.[4]

In the case of continuous Fe films square hysteresis loops with either one or two large magnetization switchings are reported in most published works, depending on the relative orientation of the applied field with respect to the magnetocrystalline easy axes, and on the existence of additional anisotropy contributions caused by surface or morphological effects. The reversal mechanism of these films can be interpreted on the basis of the occurrence of reversible rotations and irreversible magnetization jumps, strongly dependent on the effective anisotropy energy. In this frame, several papers present energetic considerations that account for most of the observed features of the hysteresis loops.[5–10]

On the other hand, magnetostatic energy and dipolar interactions play a fundamental role in the reversal mechanisms of patterned films and nanoelements of the type of those being considered as candidates for the implementation of novel recording media.[11–14] Interesting anisotropy energy terms may appear such as the so-called configurational anisotropy energy,[15] a shape effect linked to the small perturbations from uniform magnetization taking place in nonellipsoidal nanomagnets. These local shape anisotropies, as well as the collective behavior due to dipolar interactions, bring about different magnetization configurations that are relevant for the magnetization reversal. Examples of this are the local and/or global inhomogeneous remanent states (e.g., leaf or flower states).[12,16]

Within this scope, the aim of this work is to follow the evolution of the magnetization processes of a series of epitaxial Fe/MgO/GaAs heterostructures with morphologies evolving from (i) a single-crystalline smooth continuous film to (ii) continuous films characterized by the presence of morphological features (either pinholes or linear ''defects'') homogenously distributed and, finally, to (iii) tiled films formed by well separated platelets (either rounded or composed of rectangular units). We have analyzed the effective anisotropy of all samples, by means of the transverse initial susceptibility technique (hysteresis independent), and the angular dependence of the hysteresis processes.

II. EXPERIMENT

Fe(001) films were grown at different temperatures onto MgO buffered GaAs (001) substrates. The substrates were previously conditioned by growing a 2000-Å-thick GaAs epitaxial layer by molecular beam epitaxy (MBE) to planarize the surface, and then transferred on to a chamber with a combination of pulsed laser ablation (PLD) and triode sputtering systems. An 80-Å-thick MgO buffer layer was subsequently deposited by PLD (ArF excimer laser, $\lambda = 193$ nm, 17-ns pulses, 10-Hz repetition rate) at 400 °C and under a pressure of 7×10^{-9} mbar, in order to avoid the intermixing of the Fe and the GaAs and also to provide a proper symmetry and lattice match for the Fe layers.[17] The Fe(001) films, 200 Å thick, were deposited at temperatures ranging from

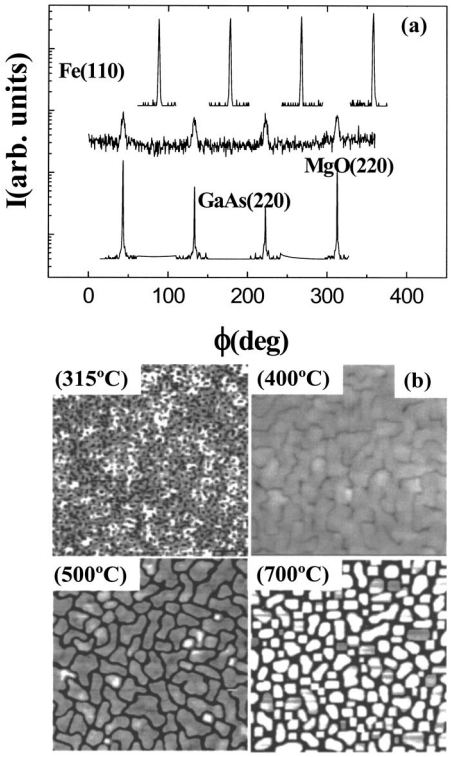

FIG. 1. X-ray diffraction ϕ scans of asymmetric reflections for a typical 200-Å Fe layer onto MgO-buffered GaAs substrate (a); AFM images ($2.5\times2.5\,\mu$m each; 20 nm height from black to white) for a series of Pt/Fe/MgO/GaAs(001) samples with Fe layers deposited at different temperatures (b).

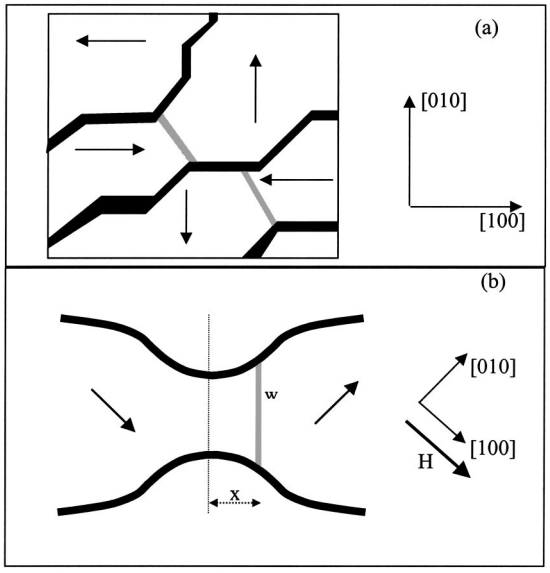

FIG. 2. Sketch showing examples of channels (black lines) and domain walls (gray lines) in the sample deposited at 400 °C (a); simplified model of a bottleneck between two channels with a 90° wall (b).

room temperature (RT) to 700 °C by triode sputtering under 4×10^{-4} mbar Ar atmosphere. A 25-Å-thick Pt capping layer was finally deposited, also by triode sputtering, to prevent oxidation of the Fe layer.

The structure and crystallinity of the samples was analyzed *in situ*, by high-energy electron diffraction (RHEED), and *ex situ* by x-ray diffraction (XRD) using Cu-K_α radiation. The RHEED patterns evidenced the occurrence of the MgO(001)[100]‖GaAs(001)[100] and Fe(001)[110]‖MgO(001)[100] epitaxial relations, independently of the deposition temperature. Figure 1(a) shows the XRD ϕ scans of the Fe(110), MgO(220), and GaAs(220) peaks that confirm the epitaxial relations previously mentioned and evidence the rotation of the Fe lattice with respect to those of MgO and GaAs. Details about the interplanar distances and lattice distortions, which were negligible in most cases and always below 0.4%, can be found in Ref. 17.

The surface morphology of the samples was studied by atomic force microscopy (AFM). The sample deposited at RT presents a continuous smooth surface with 3 Å mean roughness, approximately, while increasing temperatures lead to a gradual appearance of morphological features, as shown in Fig. 1(b). The sample prepared at 315 °C exhibits a homogeneous distribution of pinholes, with diameters between 30 and 160 nm. The sample deposited at 400 °C presents uncovered channels, usually running in zigzag, either almost parallel to the [100] and [010] axes or forming an angle of approximately 45° with those directions. The sides of neighboring channels are not usually parallel, which gives rise to the existence of ''bottlenecks'' and broadenings in the Fe deposits (see the sketch in Fig. 2). The width of the bottlenecks (broadenings) can be estimated as 100–150 nm (200–300 nm), while the distance from broadening to bottleneck is about 250 nm. Higher deposition temperatures give rise to the percolation of the channels and, consequently, to the formation of Fe platelets; the sample deposited at 500 °C shows the presence of irregular rounded islands with lateral dimensions between 200 and 700 nm, separated by distances of about 20 nm, while that deposited at 700 °C exhibits well separated platelets (interplatelet distances between 50 and 100 nm) formed by rectangular aglomerates with lateral surfaces mostly parallel to the [100] and [010] directions and sizes between 100 and 300 nm.

The magnetic properties of the films were studied at RT by transverse magnetooptic Kerr effect (MOKE) based on a semiconductor laser, colimated to about 1-mm diameter spot on the samples, and adapted to analyze the angular dependence of the magnetization process and also to measure the transverse initial susceptibility.[18,19] This technique yields the effective anisotropy of a sample by means of a measurement in an almost saturated state, i.e., independently of its magnetization reversal mechanism, and basically consists of simultaneously applying a high (saturating) dc field $H_{\rm dc}$ along either an easy or hard axis of the sample and, perpendicular to the dc field, a small ac field $h_{\rm ac}$ that induces low amplitude oscillations of the magnetization around the saturation direction. Since only reversible rotations take place, the amplitude of the oscillations, for a given ac field, depends just on the intensity of the dc field and on the magnitude of the anisotropy. For a cubic single crystal, and assuming that the magnetization is confined within the (001) plane, the anisotropy energy to first order can be written as

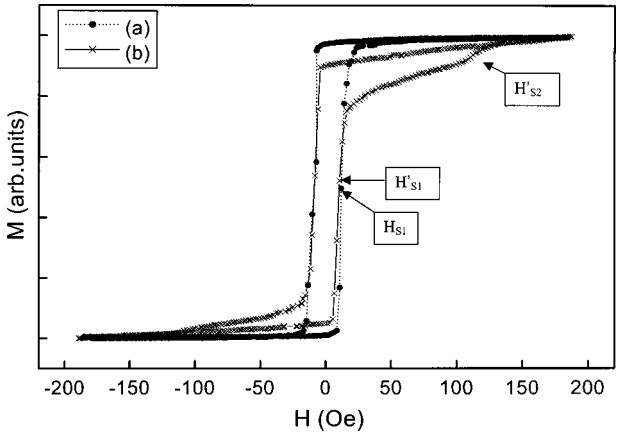

FIG. 3. Hysteresis curves of the RT deposited sample corresponding to the [100] direction (a) and to an in-plane direction 10° out of the [110] direction (b).

$$E_a = K_1 \alpha_1^2 \alpha_2^2, \tag{1}$$

where α_1 and α_2 are the director cosines of the magnetization vector with respect to the [100] and [010] axes, respectively, and K_1 is the first-order anisotropy constant. This can be referred to the angle θ between the magnetization and the [100] axis as

$$E_a = K_1 \cos^2\theta \cdot \sin^2\theta = \frac{K_1}{8}[1-\cos(4\theta)]. \tag{2}$$

The total energy of the magnetization, when $H_{\rm dc}$ is applied along an easy axis [100] and $h_{\rm ac}$ is applied perpendicular to it, includes the anisotropy energy plus the Zeeman terms corresponding to both fields,

$$E = \frac{K_1}{8}[1-\cos(4\theta)] - \mu_0 M_s H_{\rm dc}\cos\theta - \mu_0 M_s h_{\rm ac}\sin\theta, \tag{3}$$

where M_s is the saturation magnetization of the sample. By minimizing the total energy, and assuming low amplitude oscilations ($\sin\theta \approx \theta$), the transverse susceptibility χ_t can be obtained as

$$\chi_t = \frac{M_s \sin\theta}{h_{\rm ac}} \approx \frac{M_s}{H_{\rm dc}+H_K}, \tag{4}$$

where $H_K = 2K_1/\mu_0 M_s$ is the so-called effective anisotropy field, which for Fe is about 530 Oe.[20] A similar expression, but with a negative sign, can be easily obtained in case the saturating dc field is applied along an in-plane hard axis. By plotting the reciprocal transverse susceptibility χ_t^{-1} as a function of $H_{\rm dc}$, the anisotropy field H_K can be evaluated from the linear extrapolation of χ_t^{-1} to zero, by means of Eq. (4). In our case the $H_{\rm dc}$ field was applied by using an electromagnet (1 T maximum field), the transverse ac field was applied by means of a pair of Helmholtz coils operated at 383 Hz and χ_t was measured by a sincronous detection method based on a EG&G DSP lock-in amplifier.

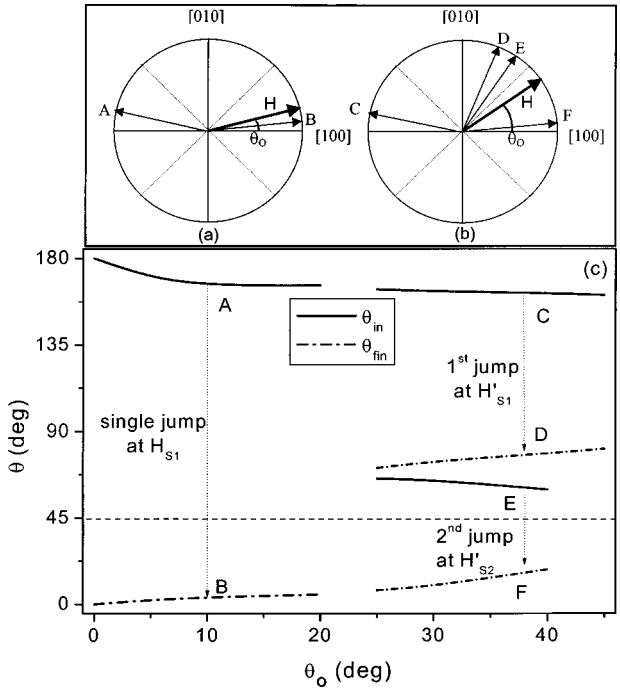

FIG. 4. Magnetization process of the RT sample (considering that the magnetization is initially in the negative [100] direction). When the field is applied very close to the positive [100] direction (a) the magnetization rotates to position A and, when the field reaches the value H_{S1}, switches irreversibly to B, from where it rotates towards the applied field. If the applied field is closer to the [110] than to the [100] direction (b) the magnetization jumps irreversibly from C to position D—between the [110] and [010] directions—when the field reaches a value H'_{S1}; then it rotates reversibly with increasing field intensity until a value H'_{S2} is reached, for which a new irreversible jump takes place, from E to F; finally it rotates towards the applied field. Graph (c) shows the initial and final angular positions of the magnetization corresponding to each irreversible jump, as a function of field direction (given by θ_0).

III. RESULTS AND DISCUSSION

We present in Fig. 3 the hysteresis loops of the sample deposited at RT—i.e., the smooth continuous film—corresponding to the field applied, respectively, along the [100] (easy) axis and to an in-plane direction slightly (10°) out of the [110] axis. The reversal process along the easy axis takes place by means of a single step at a field H_{S1}, about 10 Oe, which produces the switching of the magnetization from the $[\bar{1}00]$ to the [100] direction with no intermediate orientation. The magnetization process along the almost-hard axis shows two irreversible jumps at about 10 (H'_{S1}) and 130 Oe (H'_{S2}), respectively, and small magnetization rotations against the anisotropy field, which is characteristic of many films having fourfold anisotropy.[5–9] The magnetization process of this sample can be analyzed by studying the evolution of its energy minima as a function of the field direction and intensity. For a field applied at an angle θ_0 from the [100] easy axis (see Fig. 4), and assuming homogeneous magnetization configurations, the energy density of the film is given by

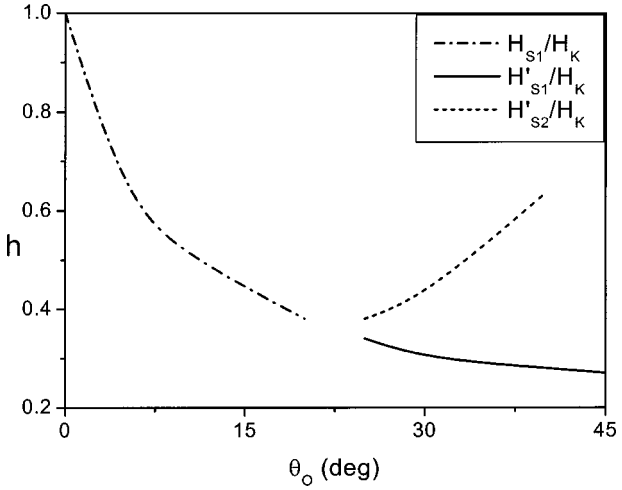

FIG. 5. Switching field values of the RT sample as a function of the field direction θ_0.

$$E = \frac{K_1}{8}[1-\cos(4\theta)] - \mu_0 M_s H \cos(\theta - \theta_0), \qquad (5)$$

where the first term corresponds to the anisotropy energy, the second to the Zeeman energy, and θ is the angle between the magnetization and the positive [100] direction. The reversal mechanism calculated from this expression is described in Fig. 4. If the magnetization initially points in the negative sense $[\bar{1}00]$ and the field is applied less than 22.5° from the [100] direction, the magnetization rotates reversibly out of the $[\bar{1}00]$ direction with increasing field [to a position such as A in Fig. 4(a)] until the field value H_{S1} is reached, then it switches to the positive sense (to position B), and finally it rotates slowly towards the field. If the field is applied at an angle between 22.5° and 45° from the [100] direction, the magnetization first carries out an irreversible jump from C to D [see Fig. 4(b)] at a field value H'_{S1}, then it rotates to E, and finally it jumps irreversibly to F—when the field reaches the value H'_{S2}—from where it rotates towards the field. Figure 4(c) shows the angles corresponding to positions A–F, as a function of the field direction, given by θ_0. The calculated values of the switching fields H_{S1}, H'_{S1}, and H'_{S2} (reduced to the anisotropy field H_K) are presented in Fig. 5. Values close to H_K and $0.3H_K$ (about 530 and 160 Oe) should be measured for H_{S1} and H'_{S1}, respectively, while H'_{S2} should be about 250 Oe, instead of the measured 130 Oe [see Fig. 3(b)]. Although the main features of the switching mechanism of this sample are accounted for in this model (the presence of either one or two jumps for θ_0, respectively, below or above 22.5°), the measured switching fields are more than one order of magnitude below the expected values. The high susceptibility associated to the jumps suggests that they take place through the propagation a few reversed nuclei by means of wall displacements, as observed by several authors.[5–7] The dispersion of switching field values present in the literature for this type of film suggests that the nucleation-propagation process is triggered from small regions in which specific conditions (e.g., high stray fields,

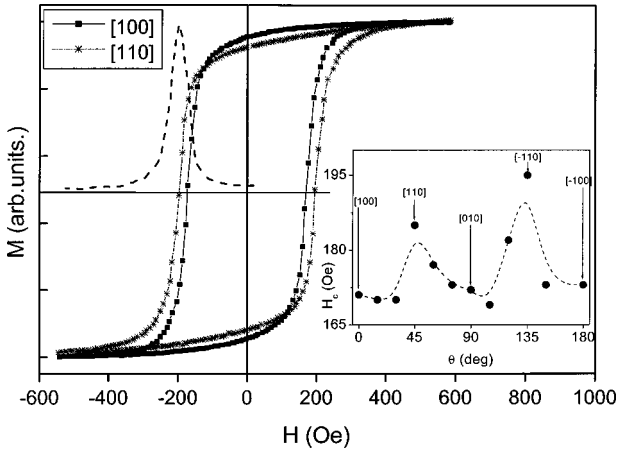

FIG. 6. Hysteresis loops of the sample deposited at 400 °C, measured along the [100] and [110] directions; the dashed line represents the differential susceptibility of the demagnetization branch of the [110] loop. The inset shows the dependence of the coercivity on the measurement direction (θ_0 is the field direction measured from the positive [100] axis; the line is a guide to the eyes).

reduced anisotropy, or local easy axes different from the global ones) could exist.

The samples characterized by the presence of a more or less homogeneous distribution of morphological features (pinholes and channels), i.e., those deposited at 315 and 400 °C, respectively, exhibit a qualitatively similar hysteresis behavior. As an example, Fig. 6 shows the hysteresis loops of the sample deposited at 400 °C, measured along the [100] and [110] directions. They present a relatively high remanence-to-saturation ratio, of about 0.9 and 0.8 for the easy and (in-plane) hard axis, respectively. The differential susceptibility of the demagnetization branch evidences a broad peak about 100 Oe wide, indicating a distribution of switching fields. The angular dependence of the coercive force (shown in the inset of Fig. 6) has a maximum, about 190 Oe, along the [110] axis, decreasing to values around 160 Oe close to the easy axis of the sample. If we take into account that the nucleation-propagation mechanism proposed for the previously analyzed (low roughness) sample yields coercivities about 10 Oe, the relatively high values obtained for this sample must be clearly linked to the presence of the above-mentioned morphological features. All experimental data are compatible with presence of domain walls: on the one hand the bottlenecks can act as pinning centers because the total energy of a wall depends on its surface area, i.e., the sample thickness times the wall width [Fig. 2(a) presents a sketch of two walls—grey lines—pinned at two bottlenecks]; on the other hand the angular dependence of the coercivity can be explained as due to the decrease of the pressure exerted by the field when it is applied out of the easy axis. A simplified model of the pinning at the bottlenecks allows an estimation of the coercive force of this sample. Figure 2(b) shows a simplified scheme of a bottleneck between two sine-shaped channels. The wall tends to remain pinned at it because in that position it has minimum area and, consequently, minimum energy. By considering the typical dimensions of the structural features (bottleneck and broadening widths,

and distance from bottleneck to broadening, as specified in Sec. II) a reasonable function for the wall width w, as a function of the distance x to the bottleneck, can be

$$w(x) = A - B\cos(2\pi x/\lambda) \tag{6}$$

with $A = 180$ nm, $B = 60$ nm, and $\lambda = 500$ nm. The energy of a wall placed at position x is

$$E_W = \gamma t w(x), \tag{7}$$

where γ is the wall energy per unit area and t is the thickness of the sample. The pinning force F_p is minus the derivative of the wall energy with respect to x and has a maximum, for $x = \lambda/4$, given by

$$F_p = -\frac{2\pi\gamma B t}{\lambda}. \tag{8}$$

When a field is applied along the [100] direction the domain at the left of the wall grows at the expense of that at the right. The force F_W exerted by the field on a 90° wall, such as that shown in Fig. 2(b), is the derivative with respect to x of the Zeeman energy,

$$F_W = \mu_o M_s H t w(x). \tag{9}$$

The coercive field is then calculated by equating the (modulus) of both expressions (the position of the wall being that corresponding to the maximum pinning force, $x = \lambda/4$, which yields $w = A$),

$$H_C = \frac{2\pi\gamma B}{\mu_o M_s \lambda A}. \tag{10}$$

By using $\gamma = 3.5\times10^{-3}$ J m^{-2} and $\mu_o M_s = 2.17$ T, which are typical values for Fe,[21] a coercivity of about 170 Oe is obtained, which is of the order of magnitude of that experimentally measured. We must mention, notwithstanding, that the γ value we have employed corresponds to 180° Fe walls; for 90° walls γ is somewhat higher due to the tilting of the wall inside the film,[21] although this does not drastically alter the order of magnitude of the coercivity. If this calculation is carried out for 180° walls a factor 2 appears in F_W that reduces the coercive force to about 85 Oe. Due to the fourfold symmetry of the anisotropy energy both 90° and 180° walls should be expected, which, in addition to the distribution of the dimensions related to the structural features, gives rise to the switching field distribution of this sample. Regarding the dipolar fields that may spring out from the poles at the walls and channel shores, they are not expected to alter the coercive force significantly; in fact dipolar fields high enough to overcome the pinning forces would produce low (semiclosed) flux configurations for low applied fields, which, in turn, would lead to low remanence configurations, which is not the case.

In the case of the sample deposited at 315 °C, whose coercivity is of the same order of magnitude, about 250 Oe, a basically similar mechanism accounts for it. The critical field H_c required to unpin a wall from an individual pinning site,

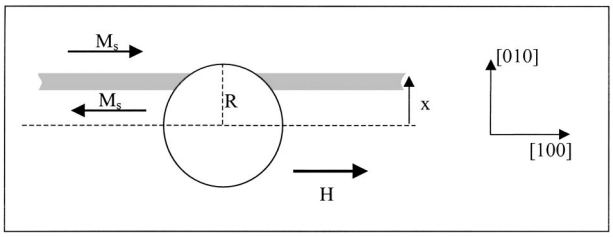

FIG. 7. Top view of cylindrical void and of a 180° wall (wide gray line) displaced a distance x from its minimum energy position, due to the pressure exerted by a field parallel to the magnetization of the domain shown in the lower part of the figure.

which in this case corresponds to a cylindrical void running from top to bottom of the film, can be calculated from the pinning force F as[22,23]

$$H_C = \frac{F}{2\mu_o M_s S}, \tag{11}$$

where S is the area of influence per pin, which can be obtained as the intervoid distance d times the film thickness t (the factor 2 in this expression corresponds to the presence of 180° walls and should be omitted for the calculations involving 90° walls). F can be calculated as the derivative of the wall energy with respect to its position x (see Fig. 7), although we must be careful since the typical wall width of Fe (of the order of 50 nm) (Ref. 21) is non-negligible with respect to the pinhole diameters (from 30 to 160 nm, as described in Sec. II). We have taken a mean pinning force value $\Delta E_w/R$, where ΔE_w is the increase in wall energy due to its increase in area when it moves from $x = 0$ to $x = R$:

$$F = \Delta E_W/R = 2\gamma t. \tag{12}$$

The factor $\beta = F/8\pi\gamma b$, where $4b$ is the interaction range of the pinning sites, which is at least equal to the size of the pinning sites, allows us to distinguish between strong ($\beta \gg 1$) and weak ($\beta \ll 1$) pinning, i.e., with or without wall deformation, respectively, prior to the wall unpinning.[23] In the case of the sample deposited at 315 °C this factor is $\beta = t/4b$ and, by taking into account its pinhole size distribution, we can conclude that we are in a weak pinning frame. The coercive force can then be calculated by introducing the value of the pinning force into expression (11), which gives

$$H_C = \frac{\gamma}{\mu_o M_s d}. \tag{13}$$

Values of a few hundred nanometers for d and those previously employed for γ (3.5×10^{-3} J m^{-2}) and $\mu_o M_s$ (2.17 T) yield again coercivities of the order of 125 Oe which also agree fairly well with the order of magnitude measured for this sample.

Regarding the magnetic anisotropy of these samples, Fig. 8 shows the transverse susceptibility plots along the easy [100] and (in plane) hard [110] axes, respectively, for the sample deposited at 400 °C. The deviation from linearity of the [110] plot for fields below 2000 Oe, approximately, is due to the fact that, contrarily to the case of the [100] plot,

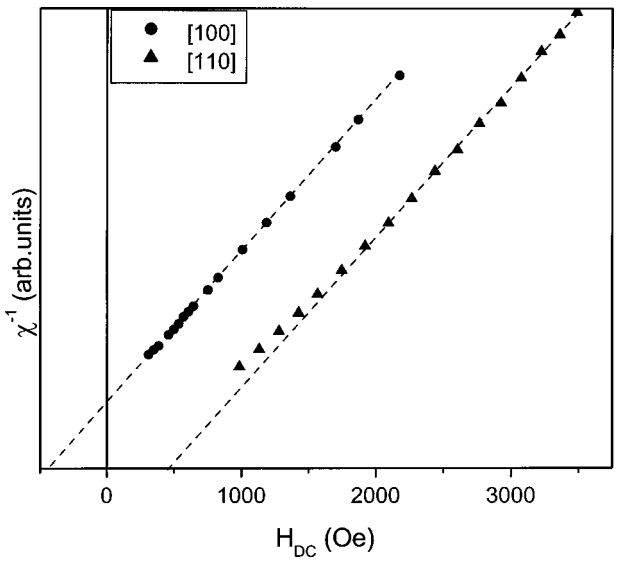

FIG. 8. Transverse susceptibility χ_t^{-1} of the sample deposited at 400 °C, measured with the saturating field H_{dc} applied along the [100] and [110] axes, respectively.

the anisotropy field pulls the magnetization vector away from saturation and, consequently, relatively large applied fields are required in order to remain in the small oscillations regime for which expression (4) is valid. From the extrapolation of χ_t^{-1} to zero an anisotropy field of almost 500 Oe is obtained, which as in the case of the RT sample yields an anisotropy constant value very close to that of bulk.

The hysteresis loops of the sample deposited at 500 °C (Fig. 9) evidence that its magnetization process takes place along a very broad field interval, as shown by the width of the differential susceptibility peak of the demagnetization branch, which enters several hundred Oe into positive field values. It is important to note that fields above 1 kOe are required in order to saturate this sample, i.e., fields much higher than the anisotropy field of iron, although its measured anisotropy constant is about 80% that of bulk. A detailed description of the magnetization mechanism of this sample would have to take into account (i) the formation of inhomogeneous magnetization states that are characteristic of nanoelements in this range of size,[12,13,16] (ii) the dipolar interactions between the nanoelements that form this sample, which cannot be excluded due to the short interplatelet separation,[12] and (iii) the broad size distribution of the platelets, from about 150 nm to almost 1 μm, which may allow the existence of domain walls in many of them.[24] However, some features of the magnetization processes of this sample can be readily analyzed: the field to saturate it can be understood as that required to overcome the demagnetizing field generated by the almost saturated platelets, which have an aspect ratio (lateral dimensions to thickness ratio) between 10 and 20; as a comparison, the demagnetizing fields for saturated oblate iron elipsoids with similar aspect ratios vary from 0.8 to 1.4 kOe. This suggests that the internal magnetostatic fields at the saturated state are probably much larger than the interplatelet interaction dipolar fields. The coercivity of this sample is somewhat lower than that of the samples deposited at 315 and 400 °C (Fig. 10), and shows a similar trend for its angular dependence, i.e., it increases when measured along the hard axis (see inset in Fig. 9); this can be understood as due to the pinning mechanism of the domain walls present at the largest platelets combined with the relatively large demagnetizing fields, which are also responsible for the lower remanence of this sample.

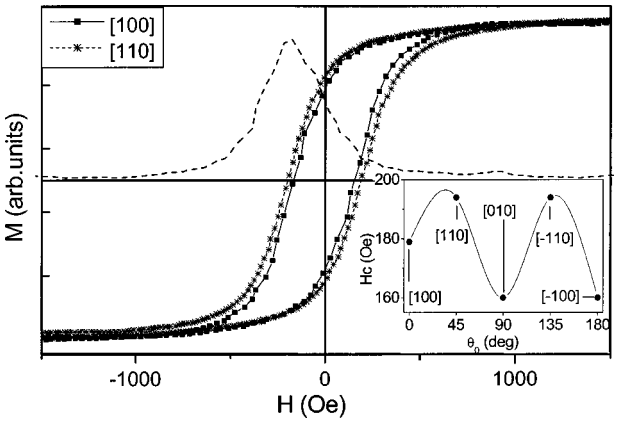

FIG. 9. Hysteresis loops of the sample deposited at 500 °C, measured along the [100] and [110] directions; the dashed line represents the differential susceptibility of the demagnetization branch of the [100] loop. The inset shows the dependence of the coercivity on the measurement direction (θ_0 is field direction measured from the positive [100] axis; the line is a guide to the eyes).

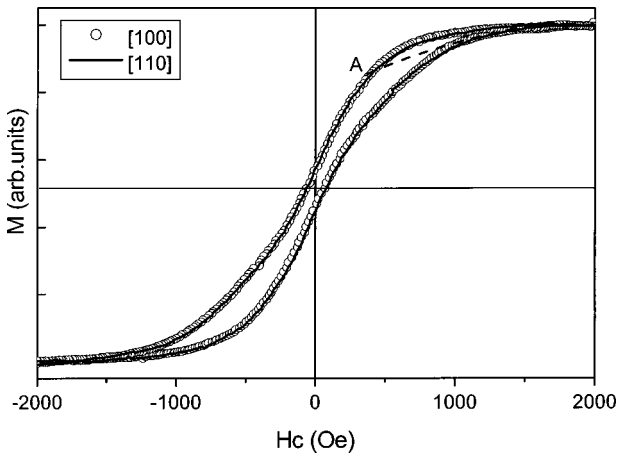

FIG. 10. Hysteresis loops of the sample deposited at 700 °C, measured along the [100] and [110] directions. When the sample is taken from positive saturation to point A and then back to positive saturation, the return path is given by the dotted line.

The most striking feature of the sample deposited at 700 °C is its isotropic hysteresis behavior, no differences being observed for any in-plane measurement direction. As an example, Fig. 10 shows the hysteresis loops corresponding to the [100] and [110] directions, which are characterized by their very low remanence, coercivity, and differential susceptibility (compared to those of the previously described samples) and high field required to saturate the sample—above 2 kOe—as well as by their constricted shape. By performing minor loops, coming down from the (positive) saturated state to a still positive field value (point A in Fig. 10)

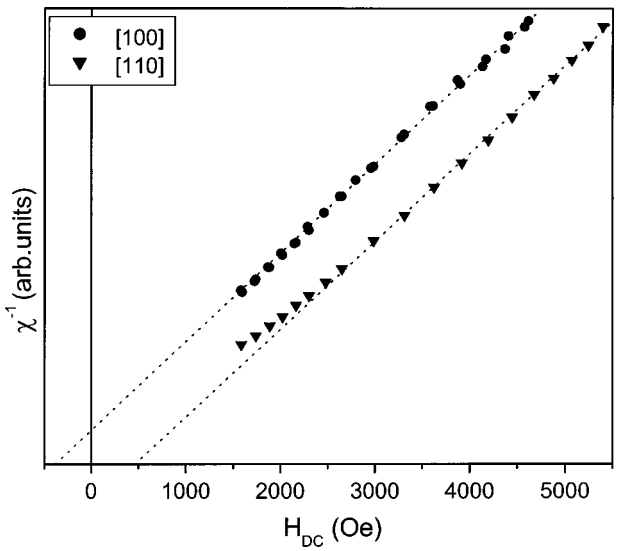

FIG. 11. Transverse susceptibility χ_t^{-1} of the sample deposited at 700 °C, measured with the saturating field H_{dc} applied along the [100] and [110] axes, respectively.

and then back to saturation it can be observed that the irreversibilities occur for very high applied fields. This suggests the presence of strong negative (demagnetizing) local fields. The larger field value required to reach saturation, compared to that of the 500 °C sample, can be clearly associated to its smaller aspect ratio, between 5 and 15, approximately. By taking into account that the islands are formed by well separated more or less square or rectangular units with lateral surfaces parallel to the [100] and [010] directions, some kind of macroscopic anisotropy should in principle be expected. In addition to the magnetocrystalline anisotropy, the configurational anisotropy reflecting the particular morphology of the islands—probably modulated by their distribution of orientation—could be present.[16] In our opinion, the isotropic hysteresis behavior of this sample indicates that the reversal mechanism is fully controlled by the dipolar interactions between the nanoelements through the nucleation and expansion of closed or semiclosed flux structures, probably involving sets of coupled islands. In fact, closed flux structures grouping sets of islands tend to increase the uniformity of the magnetization inside the individual platelets and, consequently, to reduce the eventual existence of shape induced configurational anisotropy. To clarify this point transverse susceptibility measurements were carried out because they are performed in a saturated state, i.e., the sample is uniformly magnetized to a high degree. Figure 11 shows the χ_t^{-1} versus H_{dc} plot for the [100] and [110] axes; from this figure it is evident that there is a clear anisotropy that is not apparent in the hysteresis loops. The anisotropy constant for this sample, calculated from the anisotropy field obtained from the extrapolation of χ_t^{-1} to zero and by using the saturation magnetization bulk value, is about 3.0×10^4 J m^{-3}. This reduction of the measured effective anisotropy constant with respect to that of bulk, about 34%, can be due to several factors: first, the larger magnitude of the dipolar stray fields originated by the presence of edges and corners in the platelets; second, the good crystalline quality of the lateral surfaces which, presumably, results in a larger contribution of the surface anisotropies; third, the possibility that the magnetization comes out of plane during its measurement oscillations due to the lower aspect ratio of the platelets.

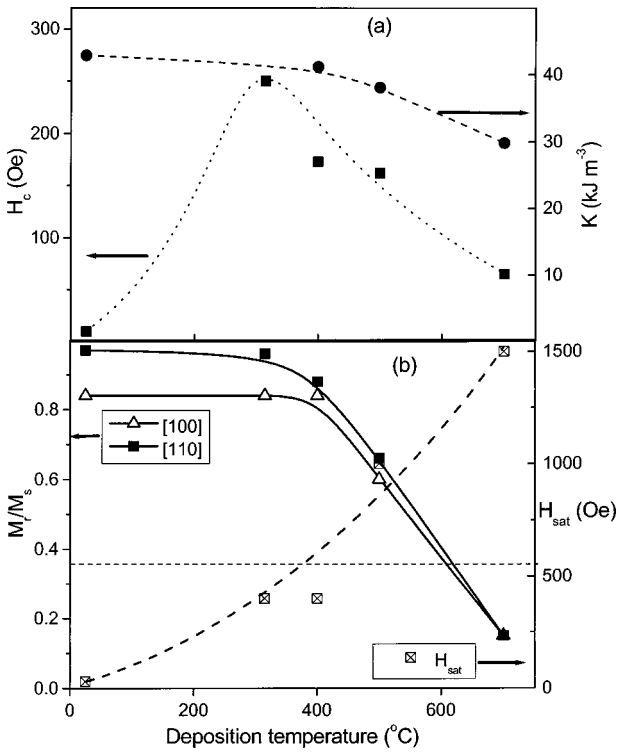

FIG. 12. Coercivity H_C—measured along the respective easy axes of the samples—and effective anisotropy constant K, as a function of the deposition temperature (a). Reduced remanence (M_R/M_s) along the [100] and [110] directions and field required to saturate the samples H_{sat}, as a function of their respective deposition temperatures (b).

IV. CONCLUSIONS

We have analyzed in this paper the evolution of the magnetization reversal processes and of the effective anisotropy of a series of epitaxial Fe/MgO/GaAs thin films deposited at increasing substrate temperatures, from RT to 700 °C, which gives rise to a gradual variation of the morphology, from continuous single-crystalline films to tiled films composed of separated platelets.

We have measured their effective anisotropy constant by means of the transverse initial susceptibility method, which is carried out by keeping the samples at an almost saturated state, thus yielding results that are independent of their specific reversal mechanisms. We have shown that the effective anisotropy is basically dominated by the bulk magnetocrystalline anisotropy of Fe, as shown in Fig. 12(a), although a small decrease in the measured values is observed for the platelet formed samples (those deposited at 500 and 700 °C, respectively) that can be due to either structural or experimental reasons already discussed. No other kind of anisotropy, related either to the particular morphology of the samples or to the eventual presence of stresses induced by

lattice mismatches between the buffer layer and samples, was found to be relevant.

The specific mechanism of magnetization reversal of each sample is extremely dependent on its particular morphology, as expected; this leads to a wide variation of the typical parameters involved in the hysteresis properties, as shown in Fig. 12. The continuous film exhibits square loops (reduced remanence close to 1 along the easy axis) whose reversal takes place by just one or two sharp magnetization jumps and reversible rotations against the anisotropy field. The low coercive forces measured, as compared to those theoretically expected, suggest that the switching mechanism is based on nucleation propagation of small reversed magnetization regions. In contrast with this, the hysteresis loops of the samples deposited at 315 and 400 °C have lower remanence-to-saturation ratio and wider distribution of switching fields, with coercivities between 150 and 250 Oe, approximately. All experimental evidences, including the dependence of the coercivity on the measurement direction, indicate that the reversal of the magnetization is hindered by the distribution of morphological defects present in these samples that act as pinning centers for the wall displacements. The sample composed of rounded islands (deposited at 500 °C) presents a hysteresis loop with a lower remanence-to-saturation ratio and a wider susceptibility peak; the field required to saturate it, higher than the anisotropy field of iron, indicates the relevance of dipolar fields in its magnetization process. At the same time, the angular dependence of the coercive force, that shows a similar trend to that of the sample deposited at 400 °C, suggests that the eventual presence of some walls cannot be disregarded. The magnetization process of the sample deposited at 700 °C, which is composed of rectangular nanoelements, shows a fully isotropic hysteresis behavior, in spite of its effective anisotropy and of its well defined crystalline order. Its very low remanence, about $0.1M_s$, the high field required to saturate it (more than four times the anisotropy field of Fe), and the presence of high-field irreversibilities suggest that the magnetization and demagnetization process is almost fully controlled by the evolution of inhomogeneous magnetization configurations, probably involving groups of nanoelements, controlled by dipolar fields.

To summarize, we have shown that the growth of Fe/MgO/GaAs samples at different temperatures results in a range of different local morphologies on the scale of the hundreds of nm. At the saturated state, the magnetic behavior of these samples essentially corresponds to that of single-crystalline bulk Fe, in good agreement with structural data. Differently from this and due to their local morphology, the magnetization reversal properties of the samples evolve from a nucleation-propagation mechanism, to pinning, and, finally, to a magnetostatically controlled process.

ACKNOWLEDGMENTS

The authors thank E. Navarro for the AFM measurements and the Spanish CICyT for financial support.

*Corresponding author. Fax: +34-913367841. Email address: fede@euitt.upm.es

[1] G. Prinz and K. Hathaway, Phys. Today **48** (4), 24 (1995).
[2] G. A. Prinz, J. Magn. Magn. Mater. **200**, 57 (1999).
[3] See, e.g., J. Magn. Magn. Mater. **200**, (1-3) (1999).
[4] *Science and Technology of Nanostructured Magnetic Materials*, edited by G. C. Hadjipanayis and G. A. Prinz (Plenum, New York, 1991).
[5] C. Daboo, R. J. Hicken, E. Gu, M. Gester, S. J. Gray, D. E. P. Eley, E. Ahmad, J. A. C. Bland, R. Ploessl, and J. N. Chapman, Phys. Rev. B **51**, 15 964 (1995).
[6] R. P. Cowburn, S. J. Gray, J. Ferré, J. A. C. Bland, and J. Miltat, J. Appl. Phys. **78**, 7210 (1995).
[7] U. Ebels, A. O. Adeyeye, M. Gester, R. P. Cowburn, C. Daboo, and J. A. C. Bland, Phys. Rev. B **56**, 5443 (1997).
[8] S. M. Jordan, J. F. Lawler, R. Schad, and H. van Kempen, J. Appl. Phys. **84**, 1499 (1998).
[9] M. Gester, C. Daboo, R. J. Hicken, S. J. Gray, A. Ercole, and J. A. C. Bland, J. Appl. Phys. **80**, 347 (1996).
[10] Yu V. Goryunov, N. N. Garyf'anov, G. G. Khaliullin, I. A. Garifullin, L. T. Tagirov, F. Schreiber, Th. Muge, and H. Zabel, Phys. Rev. B **52**, 13 450 (1995).
[11] D. Weller and A. Moser, IEEE Trans. Magn. **35**, 4423 (1999).
[12] J. Raabe, R. Pulbwey, R. Sattler, T. Schweinböch, J. Zweck, and D. Weiss, J. Appl. Phys. **88**, 4437 (2000).
[13] R. E. Dunin-Borkowski, M. R. McCartney, B. Kardynal, and D. J. Smith, J. Appl. Phys. **84**, 374 (1998).
[14] R. P. Cowburn, D. K. Koltsov, A. O. Adeye, H. E. Welland, and D. M. Tricker, Phys. Rev. Lett. **83**, 1042 (1999).
[15] R. P. Cowburn, A. O. Adeye, and H. E. Welland, Phys. Rev. Lett. **81**, 5414 (1998).
[16] R. P. Cowburn and H. E. Welland, Appl. Phys. Lett. **72**, 2041 (1998).
[17] C. Martínez-Boubeta, E. Navarro, A. Cebollada, F. Briones, F. Peiró, and A. Cornet, J. Cryst. Growth **226**, 223 (2001).
[18] J. Alameda and F. López, Phys. Status Solidi A **69**, 757 (1982).
[19] J. M. González and J. L. Vicent, J. Appl. Phys. **57**, 5400 (1985).
[20] B. D. Cullity, *Introduction to Magnetic Materials* (Addison-Wesley, Reading, MA, 1972), p. 233.
[21] S. Chikazumi, *Physics of Magnetism* (Wiley, New York, 1964), p. 186 ff.
[22] M. Kersten, Phys. Z. **44**, 63 (1943).
[23] P. Gaunt, Philos. Mag. B **48**, 261 (1983).
[24] B. D. Cullity, *Introduction to Magnetic Materials* (Addison-Wesley, Reading, MA, 1972), p. 398.